Decoupling Active Sites Enables Low-Temperature Semi-Hydrogenation of Acetylene

Journal:	*ACS Catalysis*
Manuscript ID	cs-2023-05508x.R2
Manuscript Type:	Article
Date Submitted by the Author:	27-Dec-2023
Complete List of Authors:	Li, Zhengwen; Tsinghua University, Department of chemical engineering Zhang, Jiajun; Tsinghua University, Department of Energy and Power Engineering Tian, Jiaming; Tsinghua University, Department of Chemical Engineering Feng, Kai; Tsinghua University, Department of Chemical Engineering Chen, Yuxin; Tsinghua University, chemical engineering Li, Xiao; Institute of Physics Chinese Academy of Sciences Zhang, Zhihe; Tsinghua University, Department of Chemical Engineering Qian, Shuairen; Tsinghua University, Department of Chemical Engineering Yang, Bin; Tsinghua University, Energy and Power Engineering Su, Dong; Chinese Academy of Sciences Institute of Physics, Institute of Physics, Chinese Academy of Sciences Luo, Kai Hong; University College London, Department of Mechanical Engineering Yan, Binhang; Tsinghua University, Department of Chemical Engineering

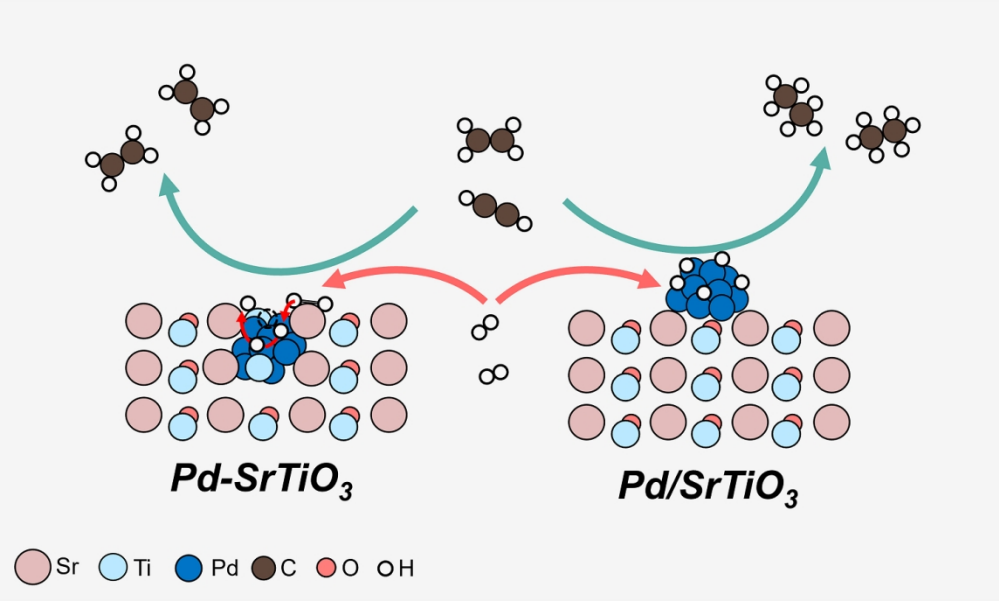

76x45mm (500 x 500 DPI)

Decoupling Active Sites Enables Low-Temperature Semi-Hydrogenation of Acetylene

Zhengwen Li[1,#], Jiajun Zhang[2,3,#], Jiaming Tian[1], Kai Feng[1], Yuxin Chen[1], Xiao Li[3], Zhihe Zhang[1], Shuairen Qian[1], Bin Yang[3], Dong Su[4], Kai Hong Luo[5], Binhang Yan[1,*]

[1] Department of Chemical Engineering, Tsinghua University, Beijing 100084, China

[2] National Engineering Research Center of Green Recycling for Strategic Metal Resources, Institute of Process Engineering, Chinese Academy of Sciences, Beijing, 100190, China

[3] Center for Combustion Energy, Key Laboratory for Thermal Science and Power Engineering of Ministry of Education, International Joint Laboratory on Low Carbon Clean Energy Innovation, Tsinghua University, Beijing 100084, China

[4] Beijing National Laboratory for Condensed Matter Physics, Institute of Physics, Chinese Academy of Sciences, Beijing 100084, China

[5] Department of Mechanical Engineering, University College London, London WC1E 7JE, United Kingdom

[#] These authors contributed equally to this work.

[*] Corresponding author: binhangyan@tsinghua.edu.cn (B. Yan)

ABSTRACT

Achieving high ethylene selectivity while preserving high reactivity for semi-hydrogenation of acetylene over Pd-based catalysts is still challenging. Here, we propose a structure of encapsulated Pd nanoparticles to enhance catalytic performance via a low-dose doping-segregation strategy using Pd-doped $SrTiO_3$ as precursor. The encapsulated Pd nanoclusters are revealed to be protected by a thin TiO_x shell to prevent contact with acetylene/ethylene. However, hydrogen can still be efficiently activated on the encapsulated Pd sites and react with the adsorbed acetylene on surface Ti^{3+} sites via hydrogen spillover. By taking advantage of weaker ethylene adsorption on partially reduced oxide TiO_x, this catalyst shows enhanced performance of 98% conversion and 92% selectivity with a specific activity of 5552 $mol_{C2H2} \cdot mol_{Pd}^{-1} \cdot h^{-1}$ at 100 ℃, significantly surpassing most Pd-based catalysts. This strategy decouples active sites for the activation of different reactants, providing a thought for the development of highly active and selective hydrogenation catalysts.

KEYWORDS: Semi-hydrogenation of acetylene, Doping-segregation, Decoupled active sites, Hydrogen spillover, Pd-based catalyst

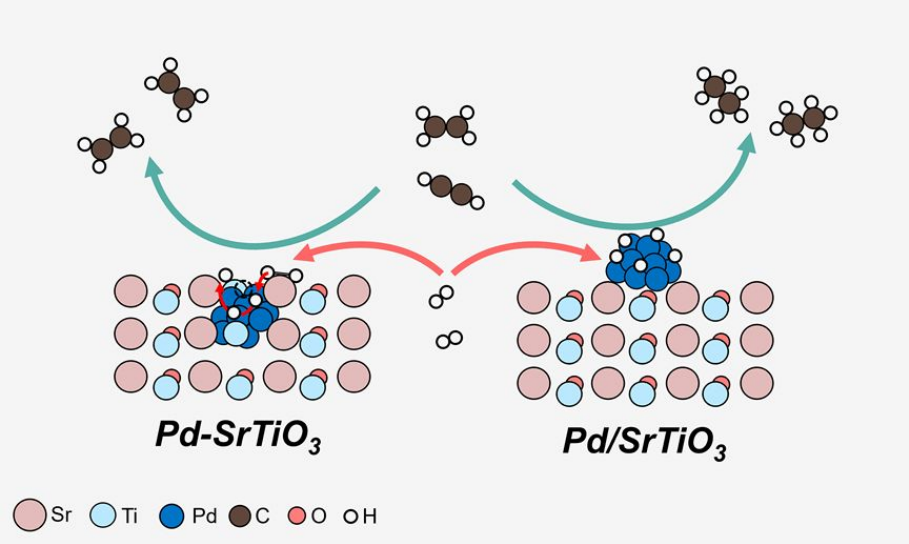

INTRODUCTION

The selective hydrogenation of alkynes to olefins is a vital process in the industrial manufacture of fine chemicals, pharmaceuticals, nutraceuticals, and agrochemicals[1-4]. Particularly, the semi-hydrogenation of acetylene under an excess ethylene flow, a crucial petrochemical process to purify alkene streams, prevents poisoning catalysts for polymerization[5,6]. Palladium serves as a highly active catalyst for this reaction, but it often leads to over-hydrogenation of acetylene to ethane and substantial wastage of raw ethylene attributed to the strong ethylene adsorption on palladium sites[7,8]. Various strategies have been explored to enhance the ethylene selectivity of Pd-based catalysts, such as downsizing Pd nanoparticles[9,10], controlling morphologies[11,12], alloying Pd with other elementals[13-16] and modifying Pd with ligands[17,18] to modify the adsorption energy of ethylene through electronic and geometric effects. However, the linear scaling relations between adsorbates pose limitations on the activation and dissociation of H_2 on palladium sites, leading to decreased hydrogenation reactivity and high reaction temperature[19,20]. Developing a catalyst with both high selectivity and high activity for semi-hydrogenation of alkynes, particularly at relatively low temperatures, remains a challenge.

Recently, reducible metal oxide materials, such as TiO_2[21], CeO_2[22], and $GaCeO_x$[23] have garnered considerable attention for enhancing alkenes selectivity due to the weak interaction of intermediates with oxygen vacancies. Nevertheless, the hydrogenation activity is orders of magnitude lower than that of metallic catalysts and a much higher reaction temperature is required owing to the sluggish H_2 dissociation dynamics[24,25]. Considering the facile H_2 dissociation on palladium sites, it inspires us to fabricate a catalyst with decoupling active sites for H_2 dissociation and C_2H_2 activation to attain both high selectivity and high reactivity for semi-hydrogenation of alkynes at relatively low temperatures. This means palladium sites should be designed only for H_2 dissociation while C_2H_2 is forced to be activated on partially reduced metal oxides such as TiO_x species. Hence, it is necessary to construct a well-defined catalyst, wherein the palladium sites responsible for H_2 dissociation are encapsulated,

which only allows the diffusion of small H_2 molecules while larger C_2H_2 molecules are restricted to be activated on the external surface of the support.

In this work, we fabricate a Pd-$SrTiO_3$ (Pd-STO) catalyst with decoupled active sites using a low-lose doping-segregation strategy of precious metals (palladium) onto perovskite precursor materials ($SrTiO_3$), demonstrating excellent potential for the encapsulated structure of segregated clusters[26,27]. The perovskite composite oxide with oxygen vacancies also delivers an excellent ability to transfer active hydrogen species at relatively mild temperatures[28]. This encapsulated structure maintains the dissociation ability for H_2 while avoiding the adsorption and over-hydrogenation of ethylene on palladium sites. Moreover, this structure takes advantage of weaker adsorption of intermediates on partially reduced oxide, TiO_x, to enhance the ethylene selectivity. Particularly, the Pd-STO catalyst shows good performance of 98% conversion and 92% selectivity with a specific activity of 5552 $mol_{C2H2}\cdot mol_{Pd}^{-1}\cdot h^{-1}$ at 100 ℃, surpassing most Pd-based catalysts reported in the literature. This demonstrated catalyst design strategy provides a thought for the development of highly active and selective hydrogenation catalysts through decoupling active sites for reactant activation.

EXPERIMENTAL SECTION

Chemicals and Materials. Strontium hydroxide octahydrate ($Sr(OH)_2\cdot 8H_2O$, >99.5%) titanium (IV) isopropoxide ($C_{12}H_{28}O_4Ti$, >99.9%), sodium tetrachloropalladate (II) (Na_2PdCl_4, >99.9%) and tungsten trioxide (WO_3, >99.8%) were supplied by Aladdin Chemical Reagent Company. Ethanol (C_2H_6O, >99.7%) was purchased from Greagent Chemical Institute. The Ar, H_2, C_2H_4 and C_2H_2 gases were all provided by Tianjin Air Liquide Gas. The above chemicals were used directly without further purification. Deionized (DI) water (resistivity: 18.2 $M\Omega\cdot cm^{-1}$) was supplied by a Milli-Q Ultrapure water system.

Catalyst Synthesis. Pd-doped $SrTiO_3$ (named Pd-STO) catalysts were synthesized using an optimized hydrothermal (HT) method, followed by calcination in air. In a typical procedure, 5.25 mmol of $Sr(OH)_2\cdot 8H_2O$ and 0.0086 mmol Na_2PdCl_4 were dissolved in 45 mL deionized water to form solution A, 5 mmol of $C_{12}H_{28}O_4Ti$ was

dissolved in 15 mL ethanol to get solution B, solutions A and B were mixed and stirred for 0.5 h, then transferred into a Teflon-lined stainless-steel autoclave and maintained at 195 ℃ for 48 h in an oven. After cooling down to room temperature, the suspensions were centrifuged, washed three times with deionized water and ethanol, and dried at 60 ℃ for 12 h. The dried powders were ground and subsequently calcined at 800 ℃ under air for 5 h in a muffle furnace to acquire the Pd-STO-C sample. The Pd-STO catalyst was finally obtained after being reduced in H_2/Ar flow at 200 ℃ for 1 h in a tube furnace.

The supported Pd/STO benchmark catalyst was synthesized by a co-impregnation method. The synthesis process of $SrTiO_3$ support was similar to that of Pd-STO without adding Na_2PdCl_4 precursor. As-synthesized $SrTiO_3$ (0.5 g) was dispersed in 60 mL deionized water, followed by dissolving 0.0043 mmol Na_2PdCl_4 and stirring treatment for 0.5 h. The suspension was continuously stirred at 80 ℃ for 5 h and dried in air at 60 ℃ for 12 h, followed by being calcined at 450 ℃ in air for 5 h in a muffle furnace to acquire the Pd/STO-C sample. The Pd/STO catalyst was ultimately obtained after being reduced in H_2/Ar flow at 200 ℃ for 1 h in a tube furnace. The palladium weight percentage for the two catalysts was kept the same.

Structural Characterization. X-ray diffraction (XRD) data were collected using an amorphous silica capillary at beamline BL14B1 of the Shanghai Synchrotron Radiation Facility (SSRF) with an X-ray wavelength of 0.6887 Å. High-resolution transmission electron microscopy (HRTEM) images were collected using a JEOL JEM-2100 transmission electron microscope. Aberration-corrected high-angle annular dark-field scanning transmission electron microscopy (HADDF-STEM) images were recorded on a FEI Titan Cubed Themis G2 300 TEM equipped with double spherical aberration correctors and an HADDF detector. Energy dispersive X-ray spectroscopy (EDS) elements mapping was carried out using the FEI TEM equipped with an energy-dispersive X-ray spectrometer (EDXS, Oxford Instrument). X-ray photoelectron spectroscopy (XPS) measurements were performed on a PHI Quantera II instrument (Ulvac-Phi, Inc.) with monochromatic Al-Kα radiation. The binding energies were calibrated based on the C 1s peak at 284.6 eV for all samples. The

palladium contents of catalysts were determined with a quadrupole spectrometer iCAP Q (Thermo Fisher Scientific) inductively coupled plasma mass spectrometry (ICP-MS). Diffuse reflectance spectra were recorded using a UV/vis/NIR spectrophotometer (UV-3600 plus, Shimadzu) equipped with a 150 mm integrating sphere. Raman spectra of catalysts were acquired on LabRAM HR Evolution with an argon laser operating at 532 nm, the in-situ Raman spectra were collected using a homemade reaction cell.

Diffuse reflectance infrared Fourier transform spectroscopy (DRIFTS) experiments were carried out in a diffuse reflectance cell (Harrick) using an FTIR spectrometer (Thermo Scientific Nicolet, iS50) equipped and a mercury-cadmium-telluride (MCT) detector cooled by liquid nitrogen. For each measurement, the sample was loaded into the in-situ reaction cell (HVC, Harrick) equipped with ZnSe windows, then reduced with H_2/Ar flow at 200 °C for 1 h and subsequently cooled to the target temperature under pure Ar flow to record background spectrum. The measurement spectra were obtained by subtracting background spectrum. Thereafter, the stream (C_2H_2/Ar = 0.2/19.8 mL·min^{-1} or CO/Ar = 10/10 mL·min^{-1}) was introduced into the reaction cell and purged away under pure Ar flow until the saturate adsorption reached. The spectra were recorded online by collecting 32 scans with a resolution of 4 cm^{-1}.

Hydrogen temperature-programmed reduction (H_2-TPR) and ethylene temperature-programmed desorption (C_2H_4-TPD) experiments were carried out on an Agilent 8860 instrument with thermal conductivity detector (TCD). For each H_2-TPR measurement, 100 mg sample was loaded into a quartz tube and pretreated at 400 ℃ for 1 h with a pure Ar flow to eliminate the surface-adsorbed species. After cooling down to 50 °C, the reactor was ramped to 350 °C in a H_2/Ar flow with a heating rate of 10 °C·min^{-1}. Prior to each C_2H_4-TPD experiment, 100 mg catalyst was loaded into a quartz tube and reduced at 200 °C with H_2/Ar flow for 1 h, and then cooled down to room temperature with a pure Ar flow. The samples were kept in a C_2H_4/Ar flow for 1 h to ensure saturated adsorption of C_2H_4. Subsequently, the weakly adsorbed C_2H_4 on catalysts was removed in a pure Ar flow at room temperature, and then C_2H_4-TPD process was conducted from 25 to 400 °C with a heating rate of 10 °C·min^{-1}. H_2-D_2

exchange experiments were performed using an online mass spectrometer (Hiden, QGA). Typically, 5 mg sample was pretreated with H_2/Ar at 200 ℃ for 1 h and cooled down to 30 ℃ under pure Ar flow. Following this, a mixture gas (H_2/D_2/Ar = 2/2/16 mL·min^{-1}) was introduced into the reaction cell and heated to 200 ℃ and the online intensity for HD (m/z = 3) was recorded.

Hydrogen Spillover Detection. Typically, 30 mg reduced sample and 1 g WO_3 powder were mixed and loaded into a quartz-tube reactor with an internal diameter of 4 mm and heated to 100 °C under Ar flow. Then, a 40 mL·min^{-1} 20% H_2/Ar flow was introduced to the reactor. After 2 h treatment, the solid sample was cooled down to room temperature and collected for observing the color change.

Catalytic Performance Evaluation. The performance evaluation was conducted in a fixed-bed quartz reactor with an inner diameter of 4 mm under atmospheric pressure[29]. For each test, 20 mg catalyst mixed with about 100 mg quartz sand was loaded into the quartz reactor and held in place with quartz wool. Before the catalytic test, the catalyst was reduced in a H_2/Ar flow at 200 °C for 1 h and then cooled to target temperature under pure Ar flow. Then the inlet flow was switched to the reactant stream (C_2H_2/H_2/C_2H_4/Ar=1:10:20:69) for C_2H_2 hydrogenation. And the space velocity was determined based on the flow rate of acetylene. The outlet gas of reactor was analyzed by an online gas chromatograph (GC-7980) instrument equipped with a flammable ionization detector (FID). The acetylene conversion and ethylene selectivity were calculated as follows:

$$C_2H_2 \text{ conversion} = \frac{F_{C_2H_2(\text{inlet})} - F_{C_2H_2(\text{outlet})}}{F_{C_2H_2(\text{inlet})}} \times 100\% \quad (1)$$

$$C_2H_4 \text{ selectivity} = \left(1 - \frac{F_{C_2H_6(\text{outlet})} + 2 \times F_{C_4(\text{outlet})}}{F_{C_2H_2(\text{inlet})} - F_{C_2H_2(\text{outlet})}}\right) \times 100\% \quad (2)$$

where F represents the mole flow rate of each substance in the inlet gas or outlet gas.

Computational Methods. The density functional theory (DFT) calculations were carried out with the dispersion corrections by the D3 method of Grimme (DFT-D3) using VASP 6.3[30,31]. The interaction between the atomic cores and valence electrons for all the elements was describe with projector augmented wave (PAW) method[32,33].

The exchange-correlation energy was calculated by generalized gradient corrected approximation (GGA) treated with the Perdew−Burke−Ernzerhof (PBE) functional[34]. The plane-wave cut-off energy was set to 450 eV for all the calculations in this study. And the Brillouin zone was sampled using a Monkhorst-Pack (2×2×1) and (4×4×1) k-points for respective geometry optimizations and static electron structure calculations. The self-consistent electronic iteration was carried out until the energy was converged to 10^{-5} eV with spin-polarized consideration. The convergence threshold of 0.03 eV/Å on maximum force was used for all the models. The results of the computational method are reliable, demonstrated by the validation of lattice constant for the perovskite lattice (primitive cell) in this study[35].

The models used for the investigation of catalytic reaction were based on a four-layer *p* (2×2) supercell of $SrTiO_3$ (110) facet. The top two layers of models were relaxed while the bottom layers were fixed during calculation. And a vacuum region of 15 Å was created above the top layer of the facet. Five Ti atoms were substituted by Pd to simulate the Pd/Ti solid solution observed in the experiment, and one O atom between Pd and Ti atoms was removed on the top layer to create the vacancy under the reductive atmosphere during reaction. The schematic diagram of surface structure was given in **Figure S22**. Geometry optimization was implemented to obtain the intermediate species for reaction modelling. The algorithm of climbing image nudged elastic band (CI-NEB) combined with the dimer method was used to determine transition state (TS)[36,37]. Vibrational analysis was carried out to confirm the transition states with only one imaginary frequency. The adsorption energy E_{ads} of species *i* was calculated as follows:

$$E_{ads,i} = E_{adsorbate,i+surface} - (E_{adsorbate,i} + E_{surface}) \quad (3)$$

where $E_{adsorbate,i+surface}$ is the total energy of surface with adsorbates, $E_{surface}$ and $E_{adsorbate,i}$ are the energies of optimized clean surface and gaseous adsorbate, respectively.

RESULTS AND DISCUSSION

Structural Characterization of Catalysts. The synthesis of palladium clusters with

encapsulated structure was realized by controlling the segregation of Pd elements within perovskite precursor, and conventional supported clusters were employed as benchmark catalysts (see Methods for details). As shown in **Figure 1a**, XRD patterns of the calcined precursors (Pd-STO-C and Pd/STO-C) show typical diffraction patterns of $SrTiO_3$, indicating that the addition of Pd does not destroy the cubic perovskite structure[38]. No crystalline palladium oxide is observed on Pd-STO-C, suggesting that Pd element is uniformly dispersed (**Figure S1**). Compared to the supported catalyst, the red shift of the adsorption edge indicates the successful doping of Pd into the lattice of $SrTiO_3$, which modifies the electronic structure of Pd (**Figure 1b**)[39]. **Figure 1c** shows the Raman spectra of $SrTiO_3$ with different doping amounts of palladium with the supported catalyst for comparison. Because of the ultra-low doping concentration of palladium (**Table S1**), the discernment of the peaks originating from atom substitution within the perovskite lattice becomes challenging. Pd-STO-H sample with a higher doping amount of palladium (~ 0.5 wt.%) was synthesized and characterized. New first-order Raman scattering peaks at 543 and 628 cm^{-1} are observed in the Pd-STO-H spectrum, indicating the successful substitutional doping of Pd atoms into the perovskite lattice by replacing Ti atoms[40]. The peak attributing to the Eg orbit of TiO_2 in the Raman spectra further confirms that the titanium atoms are replaced in the perovskite lattice[41].

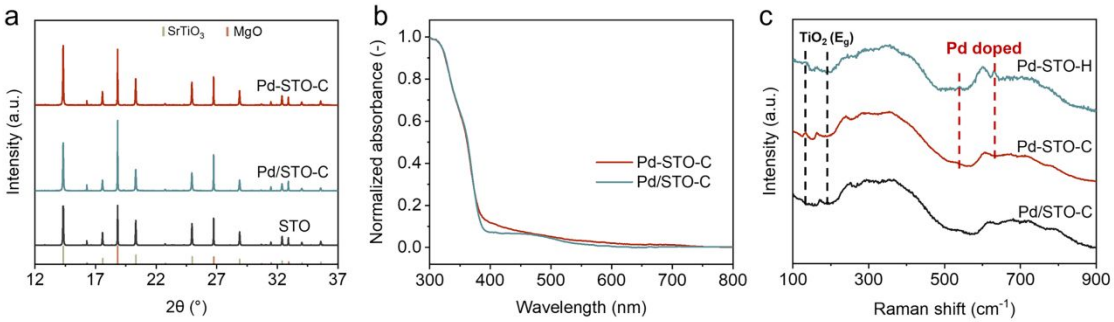

Figure 1. Structure characterization of the calcined precursors. (a) XRD spectra with MgO as the internal standard; (b) UV-Vis spectra; (c) Raman spectra.

The properties of segregated catalysts were further investigated with diverse characterization techniques. As shown in **Figure 2a, Figures S2a and S2b**, Pd clusters are uniformly localized in the $SrTiO_3$ region of Pd-STO, which is

characteristic of doping-segregation materials (**Figure S3**). Pd clusters in Pd-STO orient along the [111] direction (**Figure 2b**) and their average size is about 1.7 nm (**Figure 2c**)[42]. For Pd/STO, as shown in **Figure 2d, Figures S2c and S2d**, Pd clusters can be found at the edge of $SrTiO_3$ support, which is consistent with the characteristics of supported catalysts. The d-spacing is identified as 2.79 Å, which corresponds to the (100) facets of metallic Pd (**Figure 2e**)[43]. The average size of Pd clusters in Pd/STO is about 1.8 nm (**Figure 2f**), which is similar to that of Pd-STO and benefits for ruling out the effect of size or surface area on catalytic performance (**Figure S4**). Only the diffraction pattern of $SrTiO_3$ can be distinguished on XRD spectra also confirm the highly dispersed Pd clusters over reduced catalysts (**Figure S5**)[44]. Since CO is sensitive to the proprieties of the active metal, it was chosen as a probe molecule to investigate the spatial location of Pd clusters over the two catalysts[45]. As shown in **Figure 2g**, no signals of absorbed CO are observed for Pd-STO, suggesting the absence of active Pd sites on the catalyst surface. As a comparison, obvious peaks attributing to linear- and bridge-adsorbed CO on Pd sites suggest Pd clusters are distributed on the surface of Pd/STO. The stronger intensity of the adsorption band at 1550 ~ 1650 cm^{-1} indicates more surface defects (i.e., oxygen vacancies) on Pd-STO[46]. As shown in **Figure 2h**, the XPS data of Pd 3d orbital for the two catalysts are also quite different. The XPS peak of metallic Pd is clearly distinguished on Pd/STO, confirming that Pd clusters are loaded on the catalyst surface. In contrast, the Pd-STO catalyst exhibits an unobvious XPS signal of Pd 3d orbital, suggesting that most Pd clusters are encapsulated within perovskite[47]. Moreover, the oxidized states of Pd are observed on both calcined catalysts, indicating that the formation of the encapsulated structure is induced by the reduction process (**Figure S6**). **Figure 2i** shows the H_2-TPR curves of the calcined Pd/STO and Pd-STO catalysts. The hydrogen consumption peak centered at ~109 ℃ of Pd/STO can be assigned to the reduction of supported PdO_x clusters to metallic Pd[48]. The consumption peak of Pd-STO shifts to a higher temperature at ~182 ℃, indicating the Pd species on Pd-STO are more difficult to be reduced. This means that Pd clusters exhibit strong interaction with $SrTiO_3$ for Pd-STO, which is also a typical

characteristic of nanoparticles with an encapsulated structure[49]. Based on the above characterization results, it can be concluded that the spatial structures of Pd clusters are quite different for Pd/STO and Pd-STO catalysts.

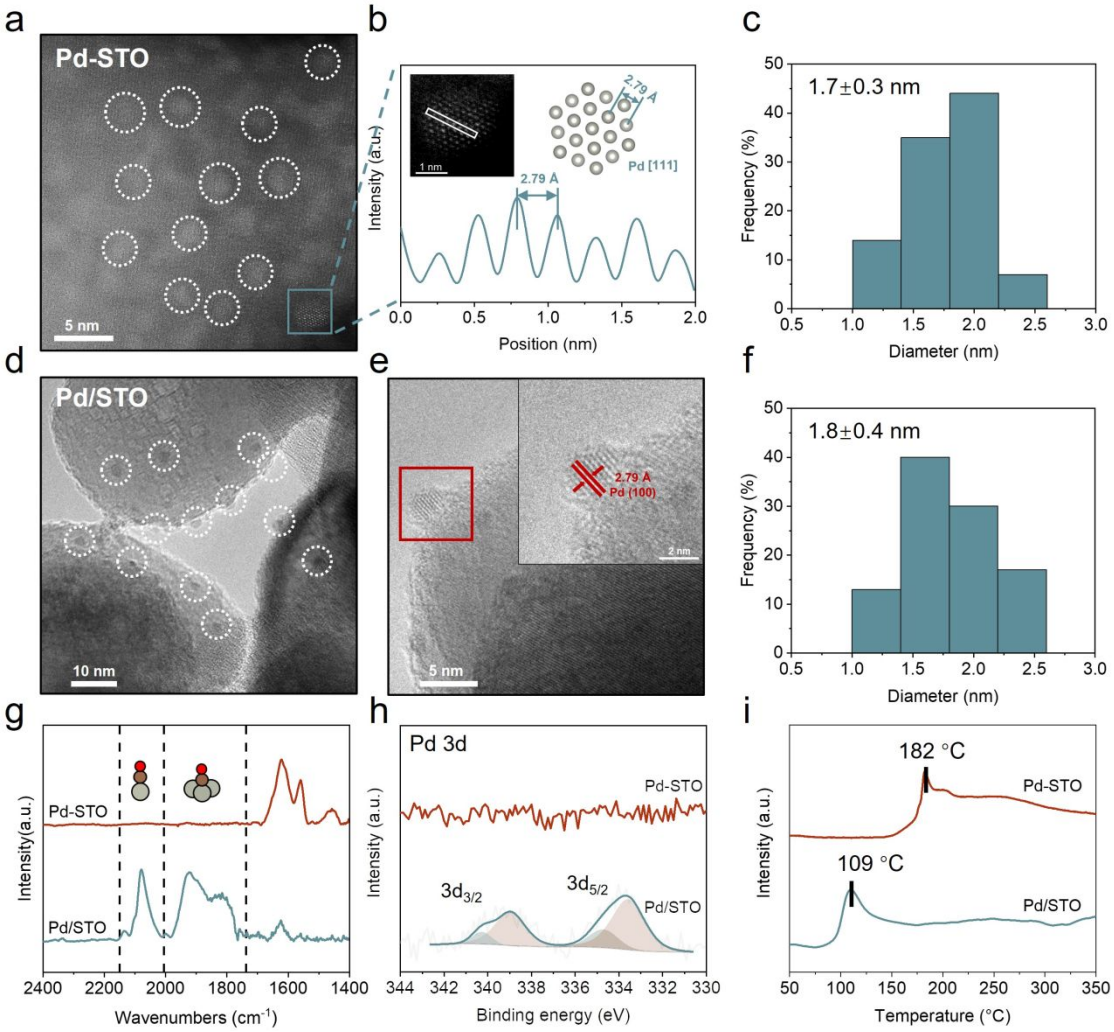

Figure 2. Structure characterization of the catalysts. (a) HAADF-STEM image of Pd-STO; (b) Intensity profiles of circled clusters; (c) Particle size distribution of Pd-STO; (d), (e) HRTEM images and (f) particle size distribution of Pd/STO. (g) CO-DRIFTS of reduced catalysts; (h) XPS Pd 3d region spectra of reduced catalysts; (i) H_2-TPR profiles of synthesized catalysts.

In order to reveal the origin of the differences in the spatial structure of Pd clusters for Pd-STO and Pd/STO, surface-sensitive Raman and XPS measurements were performed. As presented in **Figure 3a**, the calcined Pd-STO-C precursor exhibits Raman scattering peaks attributing to pristine $SrTiO_3$, indicating that the surface of Pd-STO-C is consistent with pure $SrTiO_3$ perovskite[38]. However, the reduced Pd-STO

catalyst highlights a new first-order Raman scattering peak centered at 131 cm^{-1}, suggesting that TiO_2 species appear on the surface of Pd-STO after H_2 reduction at 200 °C[41]. Given the typical strong metal-support interaction (SMSI) phenomenon observed in TiO_2-supported catalysts, partially reduced TiO_x species could cover the surface of catalysts and may be responsible for the encapsulated structure of Pd clusters in Pd-STO[50,51]. To rule out the destruction of pristine $SrTiO_3$ in the activation process to form TiO_x species, Raman spectra of Pd/STO-C reduced at various temperatures were also collected (**Figure 3b**). Only the Raman peak attributing to $SrTiO_3$ can be found, indicating that Pd/STO maintains the surface structure of $SrTiO_3$ even after high-temperature (400 °C) reduction. This also means that the TiO_2 species on the surface of Pd-STO is derived from the reduction of the special doped structure rather than from the damage of the pristine $SrTiO_3$ structure. As shown in **Figure 3c**, Ti 2p XPS peaks of reduced catalysts centered at 464.1 and 458.3 eV correspond to Ti $2p_{1/2}$ and Ti $2p_{3/2}$ of Ti^{4+} species in $SrTiO_3$, respectively. The peaks at 462.6 and 456.6 eV on Pd-STO are related to Ti^{3+} species, indicating the TiO_2 species on Pd-STO are partially reduced to form TiO_x[52]. The Sr 3d XPS spectra show Sr^{4+} in Pd-STO and Pd/STO and the O 1s XPS spectra exhibit more oxygen defect on Pd-STO with a binding energy of 530.6 eV (**Figure S7**), which is consistent with the fact that abundant Ti^{3+} species on Pd-STO[53]. The above results indicate that Pd-STO with abundant TiO_x species is formed via the reduction of the doped structure, which enables the activation of acetylene in the hydrogenation process[21].

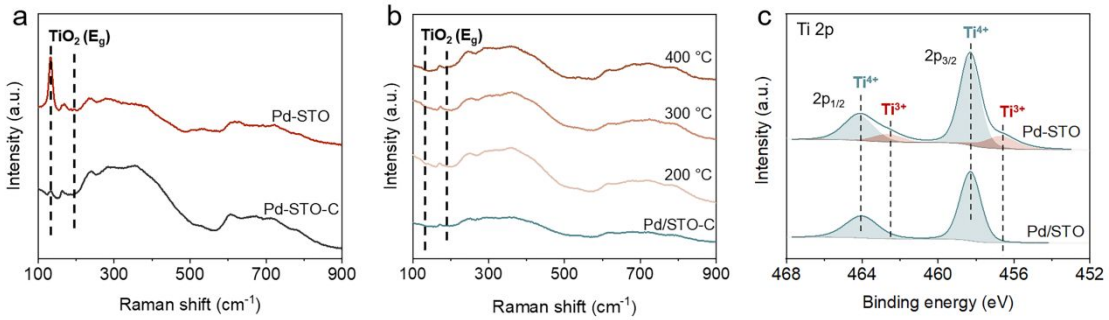

Figure 3. Surface properties of the catalysts. (a) Raman spectra of calcined Pd-STO-C and reduced Pd-STO samples; (b) Quasi in-situ Raman spectra of calcined Pd/STO-C and reduced with hydrogen at various temperatures; (c) XPS Ti 3d region spectra of reduced catalysts.

Acetylene Semi-hydrogenation Performance of Catalysts. Selective hydrogenation of acetylene over reduced catalysts was carried out to reveal the impact of the encapsulated structure of Pd clusters on catalytic performance (**Figure S8**). The relationship between acetylene conversion and ethylene selectivity with reaction temperature over Pd/STO and Pd-STO catalysts are shown in **Figures 4a and 4b**, respectively. The STO support exhibits negligible acetylene conversion over the entire reaction temperature range, indicating that $SrTiO_3$ is inert in acetylene hydrogenation (**Figure S9a**). For supported Pd species in Pd/STO, the selectivity of ethylene is below -50% when the acetylene conversion reaches 100%. The negative value of ethylene selectivity indicates that a large amount of ethylene is hydrogenated to ethane. Significantly, the Pd-STO catalyst with encapsulated Pd clusters manifests robust catalytic activity and higher ethylene selectivity than that of Pd/STO (**Figure S9b**). The selectivity towards ethylene of Pd-STO is 92 % when the conversion of acetylene reaches 98% at 100 ℃. A conventional titania-supported palladium catalyst (Pd/TiO_2), which has been reported to be a highly efficient catalyst[54,55], exhibits an inferior reactivity and selectivity compared to Pd-STO in the test (**Figures S10 and S11**). The specific activity of Pd-STO is as high as 5552 $mol_{C2H2} \cdot mol_{Pd}^{-1} \cdot h^{-1}$, surpassing most Pd-based catalysts reported in the literature (**Figure 4c**). The reaction temperature of Pd-STO is almost the lowest among the reported Pd-based catalysts, further demonstrating that Pd-STO maintains low-temperature activity while exhibits improved ethylene selectivity (**Table S2**). Besides the enhanced activity and selectivity, Pd-STO also shows good stability under the hydrogenation condition with negligible activity decay during a 60 h catalytic evaluation (**Figure 4d**), which is also validated by long-term reaction conducted at elevated space velocity of acetylene (**Figure S12**). The comprehensive characterization of the catalyst after stability test indicates the Pd-STO catalyst maintains its structural integrity throughout the reaction period (**Figures S13 and S14**). Moreover, the apparent activation energy (E_a) for acetylene hydrogenation over Pd-STO (50.4 $kJ \cdot mol^{-1}$) is comparable to that of Pd/STO (52.9 $kJ \cdot mol^{-1}$), validating that the encapsulated Pd clusters in Pd-STO maintains the comparable reactants activation capabilities to those of supported Pd

clusters (**Figure 4e**). Kinetic studies were further performed to get a deeper understanding on the C_2H_2 hydrogenation process over Pd-STO and Pd/STO catalysts. As shown in **Figure S15**, the reaction orders for C_2H_2 and H_2 over Pd-STO are -0.87 and 1.26, respectively, demonstrating that the catalyst surface is predominantly covered by adsorbed C_2H_2[56]. Moreover, the reaction orders of C_2H_2 and H_2 over Pd/STO are -0.67 and 1.95, respectively, both of which are higher than those of Pd-STO, indicating relatively stronger adsorption of C_2H_2 and C_2H_4 over Pd/STO compared with Pd-STO[57]. The kinetic studies clearly suggest a different reaction pathway on Pd-STO compared to the supported Pd/STO catalyst.

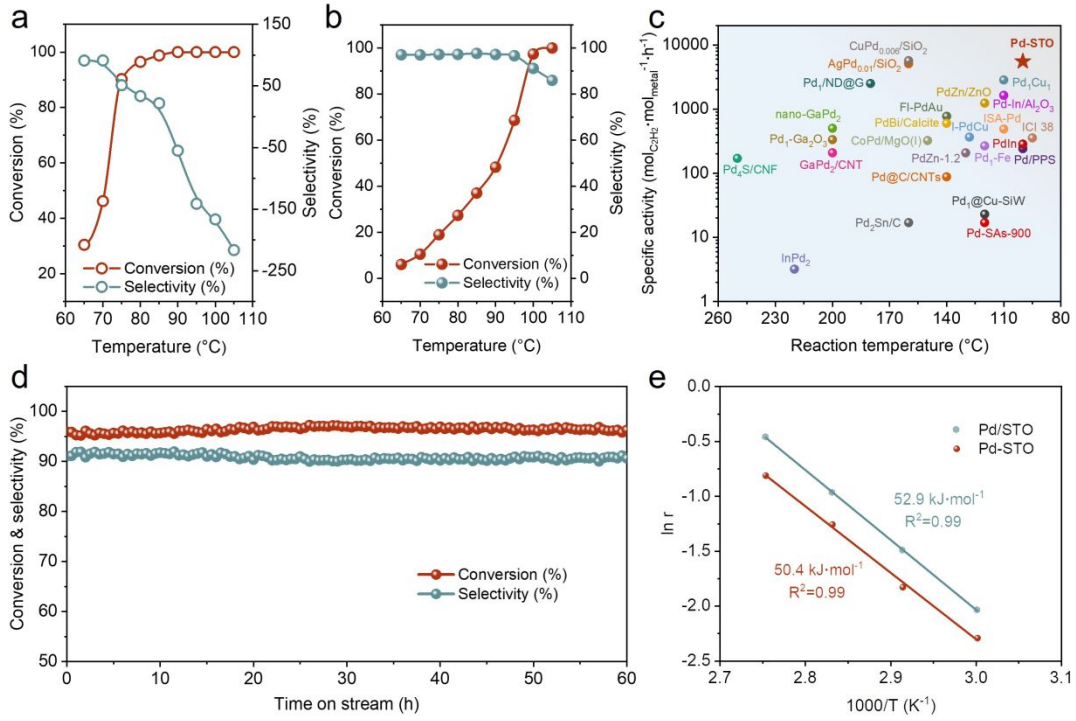

Figure 4. Catalytic performance of catalysts. (a) Conversion and selectivity as a function of reaction temperature over reduced Pd/STO, space velocity (SV) =4000 mL·g^{-1}·h^{-1}; (b) Conversion and selectivity as a function of reaction temperature over reduced Pd-STO, space velocity (SV) =1200 mL·g^{-1}·h^{-1}; (c) Relationship between the specific activity and reaction temperature of Pd-based catalysts reported in the literature and developed in this study; (d) Long-term stability test of Pd-STO under C_2H_2 hydrogenation conditions. Reaction conditions: 100 °C, $C_2H_2/H_2/C_2H_4/Ar$ = 1:10:20:69, space velocity (SV) =1200 mL·g^{-1}·h^{-1}; (e) Apparent activation energies of reduced catalysts for the semi-hydrogenation of acetylene. The apparent activation barriers were obtained at low C_2H_2 conversion to minimize the concentration gradients along

catalyst bed.

Catalytic Hydrogenation Mechanism of Catalysts. To further understand the origin of the high activity and selectivity of Pd-STO, H_2-D_2 exchange experiments were conducted to investigate H_2 activation behaviors over catalysts. As shown in **Figure 5a**, the Pd-STO catalyst reaches the maximum H_2-D_2 exchange rate at the reaction temperature of 91 ℃, which is comparable to that of Pd/STO (87 ℃), indicating that the ability to activate H_2 of encapsulated Pd clusters is the same as supported ones. The slightly lower maximum H_2-D_2 exchange rate on Pd-STO might be due to that palladium sites are partially covered by the TiO_x species, which is in agreement with the phenomena observed in catalysts with fixed or encapsulated structures[58]. Moreover, the negligible HD formation rate over STO demonstrates that $SrTiO_3$ is inert for H_2 activation. This suggests that palladium sites are indispensable for the activation of H_2 in C_2H_2 hydrogenation. Pd-STO shows a considerably low apparent activation barrier of 22.5 kJ·mol^{-1}, further validating the high H_2 activation ability of encapsulated Pd clusters (**Figure 5b**). DRIFTS were also performed to investigate the mechanism of C_2H_2 activation on Pd-STO. The time-resolved spectra of catalysts exposed under gas-phase C_2H_2 and evacuated with pure Ar are shown in **Figure 5c**. The obvious peak centered at around 731 cm^{-1} is assigned to the vibrational features ($\nu_{C\text{-}H}$) of gaseous C_2H_2[59]. After Ar evacuation, the obvious peak at 1710 cm^{-1} is the features of $\nu_{C=C}$ in adsorbed species, and the vibrational band at 1235 cm^{-1} is related to the $\nu_{C\text{-}O}$ of adsorbed species (**Figure S16**)[60]. The observation of the vibrational band of HC=CH species demonstrates the dissociated adsorption of C_2H_2 on TiO_x, forming di-σ-bonded HC=CH species with two neighboring O sites[61]. From the spectra of CO-DRIFTS, CO could not penetrate to contact with Pd due to that Pd clusters are encapsulated with TiO_x species (**Figure 2g**). The diameter of acetylene (0.38 nm) is slightly larger than that of CO (0.37 nm), indicating that C_2H_2 cannot be adsorbed and activated on Pd clusters in Pd-STO due to the hindrance of TiO_x species[46]. Clearly, acetylene hydrogenation may proceed through a completely different pathway over Pd-STO catalyst.

Since Pd clusters and TiO_x species are responsible for H_2 and C_2H_2 activation, respectively, we propose that H_2 is activated on the encapsulated Pd clusters, and then the activated hydrogen atoms diffuse to the catalyst surface to react with the adsorbed acetylene on TiO_x. To investigate the phenomenon of hydrogen spillover on Pd-STO, WO_3 was employed as a chromogenic agent as it will change from yellow WO_3 into dark H_xWO_3 after reacting with activated hydrogen species[62]. **Figure S17** exhibits the color change of the mixtures containing WO_3 and various samples before and after H_2 treatment at 100 ℃. This reaction temperature is significantly lower than that WO_3 can be reduced with gaseous hydrogen (400 ℃), which is also confirmed by the unchanged color of WO_3 during the treatment[63]. Moreover, the mixture containing Pd-STO shows a darker color than that containing Pd/STO, which can be explained by the abundant oxygen defect and partially reduced TiO_x species on the surface of Pd-STO that benefit hydrogen spillover[64]. To gain additional insights into the role of hydrogen spillover on Pd-STO, the kinetic isotope effect (KIE) for C_2H_2 hydrogenation was measured. As shown in **Figure 5d**, for Pd/STO, a k_H/k_D of 1.4 is found using H_2 or D_2 in the feed for C_2H_2 hydrogenation, in contrast, a much large KIE is observed for C_2H_2 hydrogenation over Pd-STO, with a k_H/k_D of 2.0 (**Figure 5e**). These results can be reasonably attributed to the effect of proton-assisted hydrogenation over Pd-STO, as larger deuterium species diffuse more slowly than hydrogen species in reaction.

The difference in ethylene selectivity over Pd-STO and Pd/STO catalysts was further investigated. As shown in **Figure S18a**, the peaks centered at 1620 and 1584 cm^{-1} are attributed to the π-bonded ethylene, while the peak at 1280 cm^{-1} corresponds to di-σ-bonded ethylene and ethylidyne species[65]. The interaction between C_2H_2 and surface π-bonded species is much weaker than di-σ-bonded and ethylidyne species. Therefore, the weakened ethylene adsorption on Pd-STO facilitates its desorption, resulting in higher selectivity compared to Pd/STO. Moreover, the unobvious desorption peak of C_2H_4 shown in C_2H_4-TPD profiles also indicates weaker ethylene adsorption and better C_2H_4 selectivity for Pd-STO (**Figure S18b**). These results indicate that the encapsulated Pd clusters with TiO_x species separate the ethylene and

palladium sites, thus weakening the adsorption strength of C_2H_4 on Pd-STO. Therefore, the absorbed ethylene species on Pd-STO are preferred to desorb as the target product rather than being over-hydrogenated to ethane. The surface of catalysts was further etched with a dilute nitric acid solution to understand the role of the encapsulated structure on catalytic performance. The SEM images shown in **Figure S19** demonstrate that the bulk structure of catalysts is not destroyed after etching with an acid solution. As shown in **Figure S20**, the etched Pd/STO catalyst exhibits negligible acetylene conversion over the entire reaction temperature range, indicating the dissolution loss of supported Pd clusters in acid solution. In contrast, the etched Pd-STO catalyst shows improved activity with completed acetylene conversion at 70 ℃, however, the ethylene selectivity drops to 35%. Considering the CO adsorption on Pd clusters of etched Pd-STO sample (**Figure S21**), it can be reasonably concluded that the encapsulated structure of Pd clusters of Pd-STO is destroyed due to the etching of TiO_x species in an acid solution. Therefore, acetylene and ethylene can be easily activated on palladium sites, leading to better hydrogenation activity and worse ethylene selectivity.

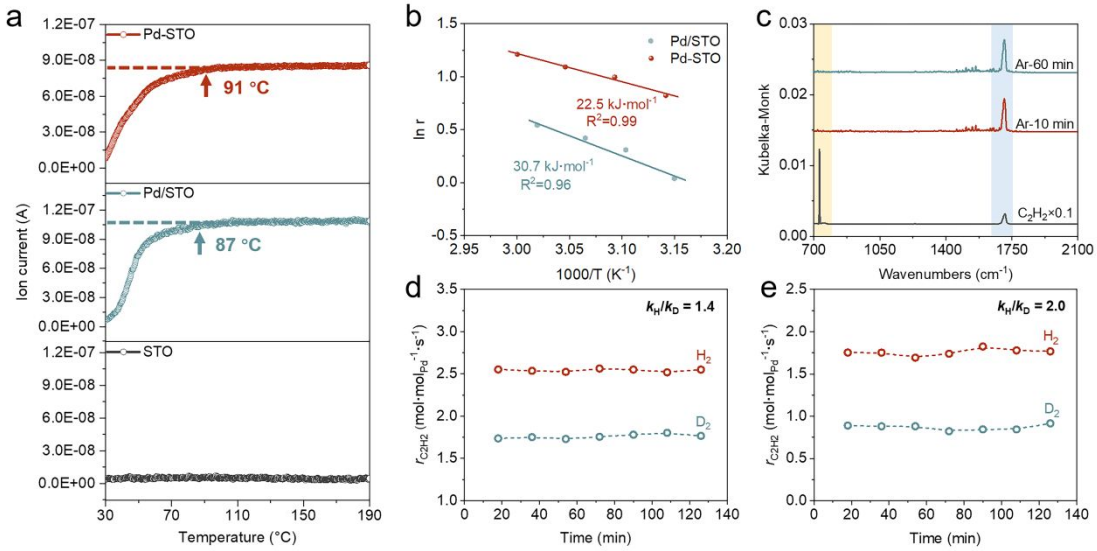

Figure 5. Insights into mechanism of C_2H_2 semi-hydrogenation. (a) H_2-D_2 exchange experiments for reduced catalysts; (b) Apparent activation energies of H_2-D_2 exchange experiments for reduced catalysts; (c) DRIFTS spectra of C_2H_2 adsorption on reduced Pd-STO; Time on stream for the C_2H_2 hydrogenation with H_2 or D_2 over reduced (d) Pd/STO and (e) Pd-STO, the reaction rates

were obtained at low C_2H_2 conversion to minimize the concentration gradients along catalyst bed.

Theoretical Insights into Hydrogenation Performance of Catalysts. Based on the above structural characterization, it can be inferred that Ti^{4+} in Pd-STO is easier to be partially reduced. This also means that the surface-coordinated oxygen is easy to be removed under a reduced atmosphere. To further demonstrate this inference, the structural property of O on the surface of Pd-STO and Pd/STO (**Figure S22**) was investigated by DFT calculations. According to the COHP analysis (**Figures 6a and 6b, Figure S23**), the Pd-O bonds of Pd-doped STO show more positive integrated projected COHPs (ICOHPs) values than Ti−O bonds in STO, indicating that the doped structure benefits for the oxygen removal process[66]. Furthermore, it is found that the Ti-O bonds on Pd-doped STO exhibit more negative ICOHPs values than that of STO, demonstrating that the introduction of Pd enhances the interaction between Ti and O atoms. The removal energy of O on Pd-doped STO and STO were also calculated, as shown in **Figure 6c and Figure S24**, the removal energy of O for Pd-doped STO is about 1.74 eV lower than that of STO, indicating that O is more easily to be removed on Pd-doped STO and this is also consistent with the experimental observations. Combined with the COHPs results, it can be inferred that the Pd-STO catalyst with Pd-O bonds destabilizes the coordinated O atoms and accelerates the removal process under a reduction atmosphere, which is contributed to abundant partially reduced TiO_x species on the Pd-STO surface.

To further understand the difference in catalytic performance of the Pd-STO and Pd/STO catalysts, the acetylene hydrogenation process was also investigated by DFT calculations. Pd-STO was modeled as $SrTiO_3$(110) with Pd atoms substitution for Ti atoms, and partially reduced Ti^{3+} sites were constructed with oxygen defects. Furthermore, exposed Pd nanoparticles on Pd/STO were modeled with Pd(111) surface. The energy profiles for acetylene hydrogenation pathways are shown in **Figure 6d**, and the top view of the geometry of intermediates is summarized in **Figures S25 and S26**. For Pd-STO, the acetylene molecule is preferentially adsorbed on the surface Ti atoms with two neighboring O sites, which is consistent with the

spectra observations. The first hydrogen atom with the absorbed acetylene molecule to form C_2H_3* with a calculated barrier of 1.05 eV (**Table S3**), which is higher than that on the surface of Pd(111). It is also consistent with the higher reaction temperature of Pd-STO compared to the Pd/STO catalyst. More importantly, the desorption of C_2H_4 from $SrTiO_3$(110) is much easier with an exothermic energy of 0.17 eV, indicating that the C_2H_4 desorption is a spontaneous process. In addition, the hydrogenation barrier for the absorbed C_2H_4 molecule to C_2H_5* is about 1.44 eV (**Figures S27 and S28**), the relatively higher energy barrier indicates that over-hydrogenation of C_2H_4 is not favorable in kinetics for Pd-STO[67]. However, the Pd(111) structure exhibits a higher ethylene adsorption energy (0.79 eV) and a lower activation energy (0.48 eV) for ethylene hydrogenation, both factors promote the hydrogenation process of ethylene and result in a waste of raw ethylene on Pd/STO. The DFT calculation results clearly indicate that Pd-STO catalysts with Ti^{3+} sites are efficient for acetylene activation, and the weak adsorption of intermediate species promotes the C_2H_4 desorption pathway.

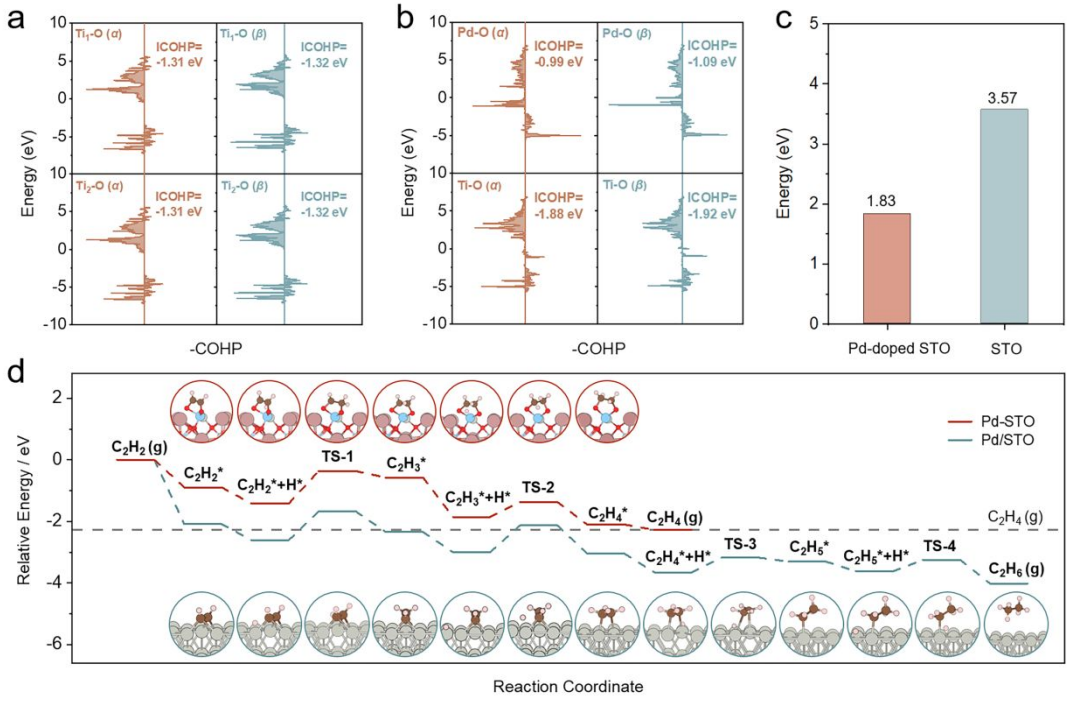

Figure 6. Theoretical insights into structure and hydrogenation mechanism. COHP analysis for the oxygen atoms in (a) STO and (b) Pd-doped STO; (c) Removal energy of oxygen on STO and Pd-doped STO; (d) Optimized surface free energy of acetylene hydrogenation pathway over

Pd-STO and Pd/STO, using the energy reference of acetylene and hydrogen molecule in the gas phase. Insets show the side view of corresponding intermediate structures. The reddish brown, light blue, red, gray, puce and pink balls denote strontium (Sr), titanium (Ti), oxygen (O), palladium (Pd), carbon (C) and hydrogen (H) atoms, respectively.

CONCLUSION

In summary, we developed an efficient Pd-STO catalyst for the low-temperature semi-hydrogenation of acetylene by a doping-segregation strategy. The Pd-STO catalyst exhibits decoupled actives sites to activate different reactants due to the encapsulated structure, where encapsulated Pd clusters and surface TiO_x species are responsible for the activation of H_2 and C_2H_2, respectively. This encapsulated structure maintains the enhanced hydrogen dissociation ability of Pd sites to preserve high activity at low temperatures, prevents Pd sites from contacting with ethylene to avoid over-hydrogenation, and takes advantage of weaker ethylene adsorption on TiO_x to enhance ethylene selectivity. The demonstrated catalyst design strategy offers insights into developing highly active and selective hydrogenation catalysts by decoupling active sites for different reactants

ASSOCIATED CONTENT

Supporting Information

The Supporting Information is available free of charge at https://pubs.acs.org/.....

HRTEM-STEM images, surface area, XRD patterns, XPS spectra, schematic of reaction apparatus, acetylene conversion and ethylene selectivity as a function of reaction temperature, stability test of catalyst, Raman spectra, CO-DRIFTS, reaction order of H_2 and acetylene, C_2H_2-DRIFTS, hydrogen spillover experiment, C_2H_4-TPD, SEM images, computational models, view of the geometry of intermediates, Gibbs free energy diagrams of hydrogenation.

ACKNOWLEDGMENTS

This work is supported by the National Natural Science Foundation of China (NSFC, Grant No. 21978148), the National Key R&D Program of China (Grant No.

2021YFA1501803) and National Natural Science Foundation of China (NSFC, Grant No. 52206156). The authors acknowledge beamline BL14B1 of the Shanghai Synchrotron Radiation Facility (SSRF) for providing the beam time and support from the UK Engineering and Physical Sciences Research Council under the project "UK Consortium on Mesoscale Engineering Sciences (UKCOMES)" (Grant Nos. EP/R029598/1 and EP/X035875/1). This work made use of computational support by CoSeC, the Computational Science Centre for Research Communities.

DECLARATION OF INTERESTS

The authors declare no competing interests.

REFERENCES

1. Zhang, L.; Zhou, M.; Wang, A.; Zhang, T. Selective hydrogenation over supported metal catalysts: from nanoparticles to single atoms. *Chem. Rev.* **2020**, *120*, 683-733.
2. Ling, Y.; Wu, Y.; Wang, C.; Liu, C.; Lu, S.; Zhang, B. Selenium vacancy promotes transfer semihydrogenation of alkynes from water electrolysis. *ACS Catal.* **2021**, *11*, 9471-9478.
3. Shi, R.; Wang, Z. P.; Zhao, Y. X.; Waterhouse, G. I. N.; Li, Z. H.; Zhang, B. K.; Sun, Z. M.; Xia, C. A.; Wang, H. T.; Zhang, T. R. Room-temperature electrochemical acetylene reduction to ethylene with high conversion and selectivity. *Nat. Catal.* **2021**, *4*, 565-574.
4. Studt, F.; Abild-Pedersen, F.; Bligaard, T.; Sørensen, R. Z.; Christensen, C. H.; Nørskov, J. K. Identification of non-precious metal alloy catalysts for selective hydrogenation of acetylene. *Science* **2008**, *320*, 1320-1322.
5. Gu, J.; Jian, M.; Huang, L.; Sun, Z.; Li, A.; Pan, Y.; Yang, J.; Wen, W.; Zhou, W.; Lin, Y.; Wang, H.-J.; Liu, X.; Wang, L.; Shi, X.; Huang, X.; Cao, L.; Chen, S.; Zheng, X.; Pan, H.; Zhu, J.; Wei, S.; Li, W.-X.; Lu, J. Synergizing metal-support interactions and spatial confinement boosts dynamics of atomic nickel for hydrogenations. *Nat. Nanotechnol*. **2021**, *16*, 1141-1149.
6. Huang, F.; Deng, Y. C.; Chen, Y. L.; Cai, X. B.; Peng, M.; Jia, Z. M.; Xie, J. L.; Xiao, D. Q.; Wen, X. D.; Wang, N.; Jiang, Z.; Liu, H. Y.; Ma, D. Anchoring Cu_1 species over nanodiamond-graphene for semi-hydrogenation of acetylene. *Nat. Commun*. **2019**, *10*, 4431.
7. Chan, C. W.; Mahadi, A. H.; Li, M. M.; Corbos, E. C.; Tang, C.; Jones, G.; Kuo, W. C.; Cookson, J.; Brown, C. M.; Bishop, P. T.; Tsang, S. C. Interstitial modification of palladium nanoparticles with boron atoms as a green catalyst for selective hydrogenation. *Nat. Commun.* **2014**, *5*, 5787.
8. Ding, L. B.; Yi, H.; Zhang, W. H.; You, R.; Cao, T.; Yang, J. L.; Lu, J. L.; Huang, W. X. Activating edge sites on Pd catalysts for selective hydrogenation of acetylene via selective Ga_2O_3 decoration. *ACS Catal.* **2016**, *6*, 3700-3707.
9. Huang, X.; Xia, Y.; Cao, Y.; Zheng, X.; Pan, H.; Zhu, J.; Ma, C.; Wang, H.; Li, J.; You, R.; Wei, S.; Huang, W.; Lu, J. Enhancing both selectivity and coking-resistance of a single-atom

Pd_1/C_3N_4 catalyst for acetylene hydrogenation. *Nano Res*. **2017**, *10*, 1302-1312.

10. Hu, M.; Wu, Z.; Yao, Z.; Young, J.; Luo, L.; Du, Y.; Wang, C.; Iqbal, Z.; Wang, X. N8 stabilized single-atom Pd for highly selective hydrogenation of acetylene. *J. Catal.* **2021**, *395*, 46-53.
11. He, Y. F.; Feng, J. T.; Du, Y. Y.; Li, D. Q. Controllable synthesis and acetylene hydrogenation performance of supported Pd nanowire and cuboctahedron catalysts. *ACS Catal.* **2021**, *2*, 1703-1710.
12. Shao, L.; Zhang, B.; Zhang, W.; Teschner, D.; Girgsdies, F.; Schlogl, R.; Su, D. S. Improved selectivity by stabilizing and exposing active phases on supported Pd nanoparticles in acetylene-selective hydrogenation. *Chem. Eur. J.* **2012**, *18*, 14962-14966.
13. Pei, G. X.; Liu, X. Y.; Wang, A. Q.; Lee, A. F.; Isaacs, M. A.; Li, L.; Pan, X. L.; Yang, X. F.; Wang, X. D.; Tai, Z. J.; Wilson, K.; Zhang, T. Ag alloyed Pd single-atom catalysts for efficient selective hydrogenation of acetylene to ethylene in excess ethylene. *ACS Catal.* **2015**, *5*, 3717-3725.
14. Zhou, H. R.; Yang, X. F.; Li, L.; Liu, X. Y.; Huang, Y. Q.; Pan, X. L.; Wang, A. Q.; Li, J.; Zhang, T. PdZn intermetallic nanostructure with Pd-Zn-Pd ensembles for highly active and chemoselective semi-hydrogenation of acetylene. *ACS Catal.* **2016**, *6*, 1054-1061.
15. Armbruster, M.; Wowsnick, G.; Friedrich, M.; Heggen, M.; Cardoso-Gil, R. Synthesis and catalytic properties of nanoparticulate intermetallic Ga-Pd compounds. *J. Am. Chem. Soc.* **2011**, *133*, 9112-9118.
16. McCue, A. J.; Guerrero-Ruiz, A.; Rodríguez-Ramos, I.; Anderson, J. A. Palladium sulphide-a highly selective catalyst for the gas phase hydrogenation of alkynes to alkenes. *J. Catal.* **2016**, *340*, 10-16.
17. Liu, K. L.; Qin, R. X.; Zheng, N. F. Insights into the interfacial effects in heterogeneous metal nanocatalysts toward selective hydrogenation. *J. Am. Chem. Soc.* **2021**, *143*, 4483-4499.
18. Albani, D.; Shahrokhi, M.; Chen, Z.; Mitchell, S.; Hauert, R.; Lopez, N.; Perez-Ramirez, J. Selective ensembles in supported palladium sulfide nanoparticles for alkyne semi-hydrogenation. *Nat. Commun.* **2018**, *9*, 2634.
19. Feng, Q. C.; Zhao, S.; Xu, Q.; Chen, W. X.; Tian, S. B.; Wang, Y.; Yan, W. S.; Luo, J.; Wang, D. S.; Li, Y. D. Mesoporous nitrogen-doped carbon-nanosphere-supported isolated single-atom Pd catalyst for highly efficient semihydrogenation of acetylene. *Adv. Mater.* **2019**, *31*, 1901024.
20. Huang, F.; Deng, Y.; Chen, Y.; Cai, X.; Peng, M.; Jia, Z.; Ren, P.; Xiao, D.; Wen, X.; Wang, N.; Liu, H.; Ma, D. Atomically dispersed Pd on nanodiamond/graphene hybrid for selective hydrogenation of acetylene. *J. Am. Chem. Soc.* **2018**, *140*, 13142-13146.
21. Wan, Q.; Chen, Y.; Zhou, S.; Lin, J.; Lin, S. Selective hydrogenation of acetylene to ethylene on anatase TiO_2 through first-principles studies. *J. Mater. Chem. A* **2021**, *9*, 14064-14073.
22. Werner, K.; Weng, X. F.; Calaza, F.; Sterrer, M.; Kropp, T.; Paier, J.; Sauer, J.; Wilde, M.; Fukutani, K.; Shaikhutdinov, S.; Freund, H. J. Toward an understanding of selective alkyne hydrogenation on ceria: on the impact of O vacancies on H_2 interaction with CeO_2(111). *J. Am. Chem. Soc.* **2017**, *139*, 17608-17616.
23. Zhou, S. L.; Gao, L. Y.; Wei, F. F.; Lin, S.; Guo, H., On the mechanism of alkyne hydrogenation catalyzed by Ga-doped ceria. *J. Catal.* **2019**, *375*, 410-418.
24. Vilé, G.; Bridier, B.; Wichert, J.; Pérez-Ramírez, J. Ceria in hydrogenation catalysis: high

selectivity in the conversion of alkynes to olefins. *Angew. Chem. Int. Ed.* **2012**, *124*, 8748-8751.

25. Wu, Z.; Cheng, Y.; Tao, F.; Daemen, L.; Foo, G. S.; Nguyen, L.; Zhang, X.; Beste, A.; Ramirez-Cuesta, A. J. Direct neutron spectroscopy observation of cerium hydride species on a cerium oxide catalyst. *J. Am. Chem. Soc.* **2017**, *139*, 9721-9727.
26. Silly, F.; Castell, M. R. Encapsulated Pd nanocrystals supported by nanoline-structured $SrTiO_3$(001). *J. Phys. Chem. B.* **2005**, *109*, 12316-12319.
27. Kim, K. J.; Han, H.; Defferriere, T.; Yoon, D.; Na, S.; Kim, S. J.; Dayaghi, A. M.; Son, J.; Oh, T. S.; Jang, H. M.; Choi, G. M. Facet-dependent in situ growth of nanoparticles in epitaxial thin films: the role of interfacial energy. *J. Am. Chem. Soc.* **2019**, *141*, 7509-7517.
28. Lu, N. P.; Zhang, Z.; Wang, Y. J.; Li, H. B.; Qiao, S.; Zhao, B.; He, Q.; Lu, S. C.; Li, C.; Wu, Y. S.; Zhu, M. T.; Lyu, X. Y.; Chen, X. K.; Li, Z. L.; Wang, M.; Zhang, J. Z.; Tsang, S. C.; Guo, J. W.; Yang, S. Z.; Zhang, J. B.; Deng, K.; Zhang, D.; Ma, J.; Ren, J.; Wu, Y.; Zhu, J. Y.; Zhou, S. Y.; Tokura, Y.; Nan, C. W.; Wu, J.; Yu, P. Enhanced low-temperature proton conductivity in hydrogen-intercalated brownmillerite oxide. *Nat. Energy* **2022**, *7*, 1208-1216.
29. Li, Z.; Zhang, J.; Tian, J.; Feng, K.; Jiang, Z.; Yan, B. Unveiling the origin of enhanced catalytic performance of NiCu alloy for semi-hydrogenation of acetylene. *Chem. Eng. J.* **2022**, *450*, 138244.
30. Kresse, G. & Furthmuller, J. Efficiency of ab-initio total energy calculations for metals and semiconductors using a plane-wave basis set. *Comp. Mater. Sci.* **1996**, *6*, 15-50.
31. Grimme, S., Ehrlich, S. & Goerigk, L. Effect of the damping function in dispersion corrected density functional theory. *J. Comput. Chem.* **2011**, *32*, 1456-1465.
32. Kresse, G. & Furthmuller, J. Efficient iterative schemes for ab initio total-energy calculations using a plane-wave basis set. *Phys. Rev. B* **1996**, *54*, 11169-11186.
33. Kresse, G. & Joubert, D. From ultrasoft pseudopotentials to the projector augmented-wave method. *Phys. Rev. B* **1999**, *59*, 1758-1775.
34. Perdew, J. P., Burke, K. & Ernzerhof, M. Generalized gradient approximation made simple. *Phys. Rev. L* **1996**, *77*, 3865-3868.
35. Mitchell, R., Chakhmouradian, A. & Woodward, P. Crystal chemistry of perovskite-type compounds in the tausonite-loparite series, $(Sr_{1-2x}Na_xLa_x)TiO_3$. *Phys. Chem. Miner.* **2000,** *27*, 583-589.
36. Henkelman, G., Uberuaga, B. P. & Jonsson, H. A climbing image nudged elastic band method for finding saddle points and minimum energy paths. *J. Chem. Phys*. **2000**, *113*, 9901-9904.
37. Henkelman, G. & Jonsson, H. A dimer method for finding saddle points on high dimensional potential surfaces using only first derivatives. *J. Chem. Phys*. **1999**, *111*, 7010-7022.
38. Enterkin, J. A.; Setthapun, W.; Elam, J. W.; Christensen, S. T.; Rabuffetti, F. A.; Marks, L. D.; Stair, P. C.; Poeppelmeier, K. R.; Marshall, C. L. Propane oxidation over $Pt/SrTiO_3$ nanocuboids. *ACS Catal.* **2011**, *1*, 629-635.
39. Yan, B. H.; Wu, Q. Y.; Cen, J. J.; Timoshenko, J.; Frenkel, A. I.; Su, D.; Chen, X. Y.; Paris, J. B.; Stach, E.; Orlov, A.; Chen, J. G. Highly active subnanometer Rh clusters derived from Rh-doped $SrTiO_3$ for CO_2 reduction. *Appl. Catal. B-Environ.* **2018**, *237*, 1003-1011.
40. Wu, Q.; Cen, J.; Goodman, K. R.; White, M. G.; Ramakrishnan, G.; Orlov, A. Understanding the interactions of CO_2 with doped and undoped $SrTiO_3$. *ChemSusChem* **2016**, *9*, 1889-1897.
41. Pan, L.; Ai, M.; Huang, C.; Yin, L.; Liu, X.; Zhang, R.; Wang, S.; Jiang, Z.; Zhang, X.; Zou,

J.; Mi, W. Manipulating spin polarization of titanium dioxide for efficient photocatalysis. *Nat. Commun.* **2020**, *11*, 418.

42. Xie, M.; Zhang, B.; Jin, Z.; Li, P.; Yu, G. Atomically reconstructed palladium metallene by intercalation-induced lattice expansion and amorphization for highly efficient electrocatalysis. *ACS Nano.* **2022**, *16*, 13715-13727.
43. Naohara, H.; Ye, S.; Uosaki, K. Epitaxial growth of a palladium layer on an Au(100) electrode. *J. Electroanal. Chem.* **1999**, *473*, 2-9.
44. Li, Z.; Lin, G.; Chen, Y.; Xue, Q.; Feng, K.; Yan, B. Regulating metal-support interactions of $Pd/MgAl_2O_4$ for efficient selective hydrogenation of acetylene. *Catal. Today* **2023,** *423*, 114253.
45. Macino, M.; Barnes, A. J.; Althahban, S. M.; Qu, R.; Gibson, E. K.; Morgan, D. J.; Freakley, S. J.; Dimitratos, N.; Kiely, C. J.; Gao, X. Tuning of catalytic sites in Pt/TiO_2 catalysts for the chemoselective hydrogenation of 3-nitrostyrene. *Nat. Catal.* **2019**, *2*, 873-881.
46. Zhang, R. D.; Teoh, W. Y.; Amal, R.; Chen, B. H.; Kaliaguine, S. Catalytic reduction of NO by CO over $Cu/Ce_xZr_{1-x}O_2$ prepared by flame synthesis. *J. Catal*. **2010**, *272*, 210-219.
47. Wang, S.; Zhao, Z. J.; Chang, X.; Zhao, J.; Tian, H.; Yang, C.; Li, M.; Fu, Q.; Mu, R.; Gong, J. Activation and spillover of hydrogen on sub-1 nm palladium nanoclusters confined within sodalite zeolite for the semi-hydrogenation of alkynes. *Angew. Chem. Int. Ed.* **2019**, *58*, 7668-7672.
48. Luo, Y. J.; Xiao, Y. H.; Cai, G. H.; Zheng, Y.; Wei, K. M. Complete methanol oxidation in carbon monoxide streams over Pd/CeO_2 catalysts: correlation between activity and properties. *Appl. Catal. B-Environ.* **2013**, *136*, 317-324.
49. Wang, H.; Gu, X. K.; Zheng, X.; Pan, H.; Zhu, J.; Chen, S.; Cao, L.; Li, W. X.; Lu, J. Disentangling the size-dependent geometric and electronic effects of palladium nanocatalysts beyond selectivity. *Sci. Adv.* **2019**, *5*, eaat6413.
50. Tauster, S. J.; Fung, S. C.; Baker, R. T.; Horsley, J. A. Strong interactions in supported-metal catalysts. *Science* **1981**, *211*, 1121-1125.
51. Yuan, W. T.; Zhu, B. E.; Fang, K.; Li, X. Y.; Hansen, T. W.; Ou, Y.; Yang, H. S.; Wagner, J. B.; Gao, Y.; Wang, Y.; Zhang, Z. In situ manipulation of the active $Au-TiO_2$ interface with atomic precision during CO oxidation. *Science* **2021**, *371*, 517-521.
52. Sun, Y.; Zhou, Y.; Liu, Y.; Wu, Q.; Zhu, M.; Huang, H.; Liu, Y.; Shao, M.; Kang, Z. A photoactive process cascaded electrocatalysis for enhanced methanol oxidation over Pt-MXene-TiO_2 composite. *Nano Res.* **2020**, *13*, 2683-2690.
53. Pan, X.; Shuai, Y.; Wu, C.; Luo, W.; Sun, X.; Zeng, H.; Bai, X.; Gong, C.; Jian, K.; Zhang, L. Switchable diode effect in oxygen vacancy-modulated $SrTiO_3$ single crystal. *Appl. Phys. A* **2017**, *123*, 1-5.
54. Guo, Y.; Huang, Y.; Zeng, B.; Han, B.; Akri, M.; Shi, M.; Zhao, Y.; Li, Q.; Su, Y.; Li, L. Photo-thermo semi-hydrogenation of acetylene on Pd_1/TiO_2 single-atom catalyst. *Nat. Commun.* **2022**, *13*, 2648.
55. Kang, J. H.; Shin, E. W.; Kim, W. J.; Park, J. D.; Moon, S. H. Selective hydrogenation of acetylene on TiO_2-added Pd catalysts. *J. Catal.* **2002**, *208*, 310-320.
56. Ma, J. M.; Xing, F. L.; Nakaya, Y.; Shimizu, K. I.; Furukawa, S. Nickel-based high-entropy intermetallic as a highly active and selective catalyst for acetylene semihydrogenation. *Angew. Chem. Int. Ed.* **2022**, *134*, e202200889.

57. Wang, C. T.; Zhang, J.; Qin, G. Q.; Wang, L.; Zuidema, E.; Yang, Q.; Dang, S. S.; Yang, C. G.; Xiao, J. P.; Meng, X. J.; Mesters, C.; Xiao, F. S. Direct conversion of syngas to ethanol within zeolite crystals. *Chem* **2020**, *6*, 646-657.

58. Cao, Y. Q.; Sui, Z. J.; Zhu, Y.; Zhou, X. G.; Chen, D. Selective hydrogenation of acetylene over Pd-In/Al_2O_3 catalyst: promotional effect of indium and composition-dependent performance. *ACS Catal.* **2017**, *7*, 7835-7846.

59. Golovkin, A.; Davlyatshin, D.; Serebrennikova, A.; Serebrennikov, L. Acetylene associates $(C_2H_2)_n$ (n=2-4) IR-spectra in argon matrixes and quantum-chemical calculations. *J. Mol. Struct.* **2013**, *1049*, 392-399.

60. Vayssilov, G. N.; Mihaylov, M.; St Petkov, P.; Hadjiivanov, K. I.; Neyman, K. M. Reassignment of the vibrational spectra of carbonates, formates, and related surface species on ceria: a combined density functional and infrared spectroscopy investigation. *J. Phys. Chem. C* **2011**, *115*, 23435-23454.

61. Cao, T.; You, R.; Zhang, X.; Chen, S.; Li, D.; Zhang, Z.; Huang, W. An in situ DRIFTS mechanistic study of CeO_2-catalyzed acetylene semihydrogenation reaction. *Phys. Chem. Chem. Phys.* **2018**, *20*, 9659-9670.

62. Xiong, M.; Gao, Z.; Zhao, P.; Wang, G.; Yan, W.; Xing, S.; Wang, P.; Ma, J.; Jiang, Z.; Liu, X.; Ma, J.; Xu, J.; Qin, Y. In situ tuning of electronic structure of catalysts using controllable hydrogen spillover for enhanced selectivity. *Nat. Commun.* **2020**, *11*, 4773.

63. Zhu, Q. Y.; Zhou, H.; Wang, L.; Wang, C. T.; Wang, H.; Fang, W.; He, M. Y.; Wu, Q.; Xiao, F. S. Enhanced CO_2 utilization in dry reforming of methane achieved through nickel-mediated hydrogen spillover in zeolite crystals. *Nat. Catal.* **2022**, *5*, 1030-1037.

64. Karim, W.; Spreafico, C.; Kleibert, A.; Gobrecht, J.; VandeVondele, J.; Ekinci, Y.; van Bokhoven, J. A. Catalyst support effects on hydrogen spillover. *Nature* **2017**, *541*, 68-7.

65. Hill, J. M.; Shen, J. Y.; Watwe, R. M.; Dumesic, J. A. Microcalorimetric, infrared spectroscopic, and DFT studies of ethylene adsorption on Pd and Pd/Sn catalysts. *Langmuir* **2000**, *16*, 2213-2219.

66. Feng, K.; Tian, J. M.; Zhang, J. J.; Li, Z. W.; Chen, Y. X.; Luo, K. H.; Yang, B.; Yan, B. H. Dual functionalized interstitial N atoms in Co_3Mo_3N enabling CO_2 activation. *ACS Catal.* **2022**, *12*, 4696-4706.

67. Ge, X.; Cao, Y.; Yan, K.; Li, Y.; Zhou, L.; Dai, S.; Zhang, J.; Gong, X.; Qian, G.; Zhou, X.; Yuan, W.; Duan, X. Increasing the distance of adjacent palladium atoms for configuration matching in selective hydrogenation. *Angew. Chem. Int. Ed.* **2022**, *134*, e202215225.